Earth and Planetary Science Letters 498 (2018) 275–287

Contents lists available at ScienceDirect

Earth and Planetary Science Letters

www.elsevier.com/locate/epsl

Stretching chemical heterogeneities by melt migration in an upwelling mantle: An analysis based on time-dependent batch and fractional melting models

Yan Liang *, Boda Liu

Department of Earth, Environmental and Planetary Sciences, Brown University, Providence, RI 02912, United States of America

ARTICLE INFO

Article history:
Received 17 November 2017
Received in revised form 9 June 2018
Accepted 28 June 2018
Available online 20 July 2018
Editor: M. Bickle

Keywords:
mantle heterogeneity
batch melting
fractional melting
decompression melting
time-dependent melting
trace element fractionation
isotope ratios
double-porosity model
dunite channel

ABSTRACT

The source region of basalt in the upper mantle is heterogeneous and may consist of depleted background mantle and blobs of enriched mantle. The size, shape, and distribution of the enriched blobs in the upper mantle are unknown but may play an important role in controlling variations in isotope ratios and trace element abundances in basalts and residual peridotites. During decompression melting, the mass flux of interstitial melt increases while the mass flux of residual solid decreases upward from the solidus, resulting in an acceleration of the effective transport velocity for an incompatible trace element in the residue. Consequently, a blob of chemical heterogeneity is stretched during its transit through the melting column. Here we quantify the melt migration induced size change by allowing trace element abundances and isotope ratios in the mantle source to vary as a function of time and space. We use simple analytical solutions for the time-dependent batch melting and fractional melting models to illustrate how a trace element or an isotope ratio varies spatially and temporally in an upwelling and chemically heterogeneous melting column. We show that an enriched blob as marked by isotope or incompatible trace element anomaly is variably stretched along the direction of melt flow during its transit through the melting column. The amount of stretching depends on the extent of melting, style of melt extraction (batch vs. fractional), porosity of the melting column, and partition coefficient, and can be quantified by a dimensionless parameter called the stretching factor. For radiogenic isotopes U, Th, Pb, Sr, Nd, and Hf, a factor of $2 \sim 8$ stretching is expected for the residue and a factor of at least 30 is found for the channel melt. For near fractional melting beneath mid-ocean ridge, an enriched Nd isotope signal takes approximately 10 times more time to transit through the low-porosity matrix than through the high-porosity channel. Hence chemical heterogeneities observed in residual peridotites and extracted melts are decoupled both spatially and temporally, which has important implications for the interpretation of isotope and trace element characteristics of the basalts and residual peridotites.

1. Introduction

Models for trace element fractionation during partial melting and melt migration are essential to the interpretation of igneous rocks. Simple melting models that have been widely used in the geochemical literature include batch melting, fractional melting, and dynamic melting models (Albarède, 1995; Shaw, 2006; Zou, 2007). These melting models were derived under the assumption of local chemical equilibrium between the partial melt and residual solid. The main difference among the three models is how much melt produced during melting remains in residual solid (also referred to as matrix hereafter). In the context of concurrent melting and melt extraction in a one dimensional (1D) steady-state upwelling column, batch melting corresponds to an endmember case in which all the melt generated in the solid matrix percolates upward through the upwelling melting column (Ribe, 1985a; Spiegelman and Elliott, 1993; Asimow and Stolper, 1999). Perfect fractional melting corresponds to an endmember case in which melt generated at any point in the upwelling column is completely and instantaneously removed from the solid matrix. In a physically more realistic setting, a fraction of melt is left behind in the melting column. In the standard treatment of dynamic or continuous melting, one assumes that a constant and small fraction of melt is retained in the residual solid (Langmuir et al., 1977; McKenzie, 1984; Albarède, 1995; Zou, 1998; Shaw, 2000). For melting in an upwelling column, the steady-state version of the dy-

---

* Corresponding author.
E-mail address: yan_liang@brown.edu (Y. Liang).

https://doi.org/10.1016/j.epsl.2018.06.042

namic melting model has the same algebraic expression for the melt composition as the standard dynamic melting model if one replaces the melt fraction in the latter by the ratio between the mass flux of the melt and the mass flux of the solid in the melting column (Liang, 2008). The melt-to-solid mass flux ratio is constant and uniform in the steady-state dynamic melting model. During concurrent melting and melt migration in a 1D steady-state upwelling column, porosity and melt velocity, hence the mass flux of the melt, increase as a function of the degree of melting or the height measured from the base of the melting column, whereas the mass flux of the solid decreases upward (Ribe, 1985a; Spiegelman and Elliott, 1993; Asimow and Stolper, 1999; Hewitt and Fowler, 2008). Iwamori (1993b, 1994) unified the steady-state batch and fractional melting models by allowing part of the melt generated in the partially molten residual mantle to segregate into its neighboring channels. The style of melting is encapsulated by a dimensionless melt suction rate ($\mathbb{R}$), defined as the rate of melt extracted from the matrix to the channel ($\dot{S}$) relative to the rate of matrix melting (Γ_m), viz.,

$$\mathbb{R} = \frac{\dot{S}}{\Gamma_m(1-\psi)}, \tag{1}$$

where ψ is the volume fraction of melt conduits or high-porosity channels in the upwelling column (Iwamori, 1994; Ozawa, 2001; Liang and Peng, 2010). For a constant melt suction rate, concentration of a trace element in the matrix melt in the melting column (C_f^m) is given by the simple expression (Iwamori, 1994)

$$C_f^m = \frac{C_s^0}{k_m}\left[\frac{k_m + (1-k_m-\mathbb{R})F}{k_m}\right]^{\frac{k_m-1}{1-k_m-\mathbb{R}}}, \tag{2a}$$

where C_s^0 is the solid concentration at the onset of melting; k_m is the bulk solid–melt partition coefficient for the trace element of interest in the matrix. The degree of melting experienced by the solid matrix, F, increases upward along the melting column. For constant melting rate, we have

$$F = \frac{\Gamma_m z}{\rho_s V_s^0}, \tag{2b}$$

where z is the vertical coordinate with origin at the bottom of the melting column and V_s^0 is the solid upwelling rate at the onset of melting ($z = 0$). Eq. (2a) recovers the batch melting model and the perfect fractional melting model when $\mathbb{R} = 0$ and $\mathbb{R} = 1$, respectively. Ozawa (2001), Liang and Parmentier (2010), and Liang and Peng (2010) further generalized Eq. (2a) by including additional sources and sinks and by considering spatially variable melt suction rate. Applications of Eq. (2a) and its more generalized versions to REE variations in clinopyroxenes in abyssal peridotites demonstrate that $\mathbb{R}$ is typically greater than 0.8 (Iwamori, 1994; Lundstrom, 2000; Ozawa, 2001; Liang and Peng, 2010), i.e., the style of melting is near fractional as originally suggested by Johnson et al. (1990).

A feature common to the aforementioned melting models is the constant and uniform source composition (C_s^0). These simple melting models are only suitable for studying melting a compositionally homogenous mantle. For example, C_s^0 could be the concentration of a trace element in the depleted MORB mantle (DMM) or an enriched mantle (EM), but not both. For melting a two-component mantle (e.g., DMM and EM), the standard geochemical treatment is mixing, either before (i.e., mixing the two sources) or after melting calculations (mixing melts derived from the two components). There is no spatial or temporal information in the mixing model. For melting an upwelling and spatially inhomogeneous mantle, such as the one shown in Fig. 1, one must consider variable or time-dependent source compositions, as different sources feeding into the melting column at different times.

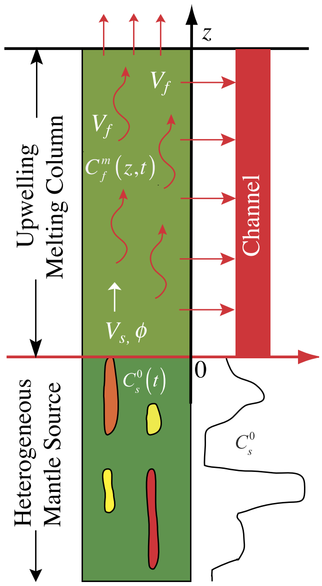

Fig. 1. Schematic diagram showing the model setup. The base of the melting column is at $z = 0$ where chemically heterogeneous sources are introduced. The background or ambient mantle source is shown in green, while the chemically heterogeneous mantle sources are marked by red, orange, and yellow blobs below the melting region ($z < 0$). Melt generated at $z \geq 0$ is allowed to segregate both vertically through the overlying melting column (matrix) and horizontally into neighboring channels. Modified after Liang (2008). (For interpretation of the colours in the figure, the reader is referred to the web version of this article.)

Richter and Daly (1989) were among the first to examine the consequences of melting a heterogeneous mantle column through time-dependent numerical simulations. DePaolo (1996) and Liang (2008) generalized the steady-state dynamic melting model by allowing trace element abundance in the source region to vary as a function of time and space. Results from these studies showed how initially correlated isotope and trace element ratios for two elements of different compatibility (e.g., Sr and Nd) are phase-shifted (in time) or decoupled (in space) as a result of chromatographic fractionation in the melting column. Under the condition of local chemical equilibrium, the effective transport velocity (V_{eff}) for a trace element in the upwelling melting column depends on solid–melt partition coefficient (k_m) and is given by the expression (McKenzie, 1984)

$$V_{eff} = \frac{\rho_f \phi_m V_f^m + \rho_s(1-\phi_m)V_s^m k_m}{\rho_f \phi_m + \rho_s(1-\phi_m)k_m}, \tag{3}$$

where ρ is density; V is velocity; and ϕ is the porosity or volume fraction of the melt in the matrix; superscript m refers to residual solid matrix; subscripts f and s stand for melt and solid, respectively. (Key symbols are listed in Table 1.) In the models of DePaolo (1996) and Liang (2008), as well as most geochemical studies of mantle chromatography (e.g., Navon and Stolper, 1987; Bodinier et al., 1990; Hauri, 1997), V_{eff} is constant and uniform in the melting column as spatial variations in porosity and melt and solid velocities are not considered. Hence the size of a chemical heterogeneity does not change during dynamic or continuous mantle melting.

In general, porosity, melt and solid velocities vary systematically during melting and melt migration in an upwelling mantle column (Ribe, 1985a; Spiegelman and Elliott, 1993; Jull et al., 2002; Hewitt and Fowler, 2008). Fig. 2a shows spatial variations of matrix porosity for several choices of the dimensionless melt suction rate

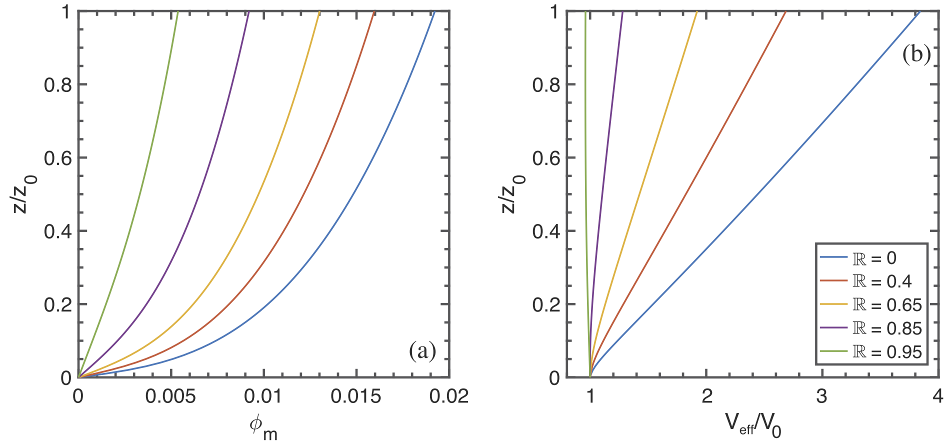

Fig. 2. Variations of porosity (a) and effective velocity (b) along the melting column for 5 choices of the melt suction rate. The extent of melting at the top of the melting column is 15%. The reference porosity is 2% and the bulk solid–melt partition coefficient is 0.03. (For interpretation of the colours in the figure, the reader is referred to the web version of this article.)

Table 1
List of key symbols.

Symbol	Description
C_f^m, C_f^{ch}	Concentration of a trace element in the matrix or channel melt
C_s^0	Concentration of the bulk solid at the onset of melting
C_{DM}^0, C_{EM}^0	Concentrations of a trace element in the depleted mantle or the enriched mantle source
F	Degree of melting experienced by the solid matrix (Eqs. (8b) and (8c))
F_d	Degree of batch melting in the lower part of the upwelling column
$F_{\max}$	Maximum extent of melting at the top of the melting column
h_0	Initial thickness of the chemical heterogeneity
$h_{stretched}^m, h_{stretched}^{ch}$	Stretched length of a heterogeneity at the top of the melting column
k_m	Bulk solid–melt partition coefficient for a trace element in the matrix
n	The exponent in the permeability model (Eq. (A.3)), $n = 3$ in this study
$\mathbb{R}$	Relative melt suction rate (Eq. (1))
R	Isotope ratio of the matrix melt or solid (Eqs. (12) and (20c))
$\dot{S}$	The rate of melt extracted from the matrix to the channel
t_0	Solid upwelling time scale, $t_0 = z_0/V_s^0$
t	Time
V_{eff}	Effective transport velocity for a trace element in the matrix (Eq. (3))
V_f^m, V_s^m	Velocity of the matrix melt or the solid
V_s^0	Solid upwelling rate at the onset of melting
z_0	Height of the column where melting takes place
z	Vertical coordinate with origin at the bottom of the melting column
ϕ_0	Matrix porosity at the top of the melting column (Eq. (A.8))
ϕ_{ref}	Reference porosity of the matrix defined by Eq. (A.5)
ϕ_m	Porosity or volume fraction of the melt in the matrix
κ_ϕ	Matrix permeability (Eq. (A.3))
Γ_m	Matrix melting rate
ρ_f, ρ_s	Density of the melt or the solid
ψ	Volume fraction of high-porosity channels in the upwelling column

in a steady-state upwelling melting column. The porosity is calculated using a double-porosity melting model (Appendix A) similar to those described in Iwamori (1993a), Lundstrom (2000), Jull et al. (2002), and Liang and Peng (2010). Porosity increases upward for a given melt suction rate $\mathbb{R}$, but decreases with increasing $\mathbb{R}$ at a given depth in the melting column. The mass fluxes of the melt and solid in the matrix depend on the extent of melting and melt extraction in the melting column, viz.,

$$\rho_f \phi_m V_f^m = \rho_s V_s^0 (1 - \mathbb{R}) F, \tag{4a}$$

$$\rho_s (1 - \phi_m) V_s^m = \rho_s V_s^0 (1 - F). \tag{4b}$$

Substituting Eqs. (4a) and (4b) into Eq. (3), we have a new expression for the effective transport velocity:

$$V_{eff} = \frac{\rho_s[(1-\mathbb{R})F + (1-F)k_m]}{\rho_f \phi_m + \rho_s(1-\phi_m)k_m} V_s^0. \tag{5}$$

For a given $\mathbb{R}$, the effective velocity of an incompatible trace element increases upward in the melting column (Fig. 2b, except the case $\mathbb{R} = 0.95$, which we will explain in this study). Hence, the size of mantle heterogeneity as marked by highly incompatible trace elements or their isotope ratios increases upward during its transit through the melting column. This has important implications for the interpretation of spatial and temporal variations in isotope and highly incompatible trace element ratios in basalts and residual peridotites as these chemical indices have been widely used to fingerprinting the nature and scale of heterogeneities in mantle sources.

Stretching chemical heterogeneity by melt migration in the mantle has not been examined before. In this study, we generalize the steady-state double-porosity melting model (Eq. (2)) by allowing the source composition feeding into the upwelling column to vary as a function of time. We use Eqs. (4a) and (4b) to calculate the melt and solid mass fluxes and obtain analytical solutions to the governing mass conservation equation for a trace element in the matrix melt and solid. We discuss the first order features of our new models and compare our results with the time-dependent dynamic melting model. We introduce a stretching factor that can be used to quantify the relative size change or deformation of a chemical heterogeneity during concurrent melting and melt migration in the mantle column. Under conditions pertinent to adiabatic mantle melting, we show that the size of the chemical heterogeneity in the matrix is increased for moderately to highly incompatible trace elements but decreased for compatible trace elements during their transport in the upwelling melting column. The sizes of the chemical heterogeneity as marked by incompatible trace elements and their isotope ratios are significantly stretched during their transit through high-porosity dunite channels.

2. Time-dependent melting in an upwelling mantle

2.1. Model setup

The basic setup of our model is shown schematically in Fig. 1. We consider melting and melt migration in a 1D upwelling column in which part of the melt generated is extracted to nearby channels. We treat the low porosity matrix (residual mantle) and high porosity interconnected channel network as two overlapping continua and use the time-dependent double-porosity model outlined in Appendix B to solve for spatial and temporal variations of a trace element in the matrix melt and the channel melt. To demonstrate the basic idea, we focus on chemical rather than lithological heterogeneity in this study. This allows us to simplify the mechanic part of the problem by assuming that the porosities, melt and solid velocities of the matrix and channel are in steady-state, and the volume fractions of the high porosity channel (ψ) are constant and uniform in the melting column. In the absence of diffusion and dispersion in the melt, the 1D mass conservation equation for a trace element in the matrix continuum takes on the form (Appendix B),

$$\left[\rho_f\phi_m+\rho_s(1-\phi_m)k_m\right]\frac{\partial C_f^m}{\partial t} + \rho_s V_s^0\left[(1-\mathbb{R})F+(1-F)k_m\right]\frac{\partial C_f^m}{\partial z} = (k_m-1)C_f^m\Gamma_m, \tag{6}$$

where t is the time. (A similar equation for the channel melt is given in Appendix B.) Eq. (6) is valid when local chemical equilibrium between the solid and interstitial melt is maintained and k_m is constant and uniform in the melting column (i.e., modal melting). The porosity and degree of melting are functions of spatial coordinate z in the upwelling column but independent of time (Fig. 1 and Eq. (2b)). Eq. (6) is a first order partial differential equation with variable coefficients and can be solved using standard methods. Below we consider a simplified model that has analytical solutions.

2.2. Time-dependent batch melting and fractional melting models

To focus on essential features of time-dependent melting while keeping the problem tractable, we assume constant melting rate and make two simplifying approximations regarding the porosity in the first term on the left hand side of Eq. (6): (i) $\phi_m \ll 1$, and (ii) $\rho_f\phi_m/\rho_s \approx \phi_0 z/z_0$, where ϕ_0 is the matrix porosity at the top of the melting column (z_0). Simplification (i) is reasonable as porosity is likely very small in an upwelling mantle column. As shown in Fig. 2a, there is significant nonlinearity in porosity in the lower most part of the melting column. The linear approximation in porosity allows us to obtain a simple analytical solution which captures the essential features of the time-dependent melting problem. This linear approximation is only applied to the first term on the left hand side of Eq. (6). The simplified version of Eq. (6) is nondimensionalized with the substitution,

$$t = t_0 t', \quad \text{and} \quad z = z_0 z', \tag{7}$$

where z_0 is the height of the column where melting takes place; and $t_0 = z_0/V_s^0$ is the solid upwelling time scale. (Note there is no advantage to scale concentration in Eq. (6).) The nondimensionalized equation, after dropping the primes, is

$$\frac{\partial C_f^m}{\partial t} + \frac{[(1-\mathbb{R})F_{\max}z+(1-F_{\max}z)k_m]}{\phi_0 z+k_m}\frac{\partial C_f^m}{\partial z} = \frac{F_{\max}(k_m-1)C_f^m}{\phi_0 z+k_m}, \tag{8a}$$

where $F_{\max}$ is maximum extent of melting at the top of the melting column,

$$F_{\max} = \frac{\Gamma_m z_0}{\rho_s V_s^0}. \tag{8b}$$

The degree of melting increases linearly in the melting column ($0 \le z \le 1$) for the case of constant melting rate,

$$F = F_{\max}z. \tag{8c}$$

Solutions to Eq. (8a) depend on the initial and boundary conditions (Appendix B). To focus on the effect of a variable mantle source composition, we consider solutions at large times (i.e., $t \ge 1$) when the original materials in the melting column have completely advected out of the system. Solution to Eq. (8a) then depends only on the boundary condition at the base of the melting column ($z = 0$), which can be written as

$$C_s(0,t) = C_s^0(t), \tag{8d}$$

where C_s^0 is a function of time. Integrating Eq. (8a) along a characteristic line, we have

$$C_f^m(z,t) = \frac{C_s^0(t-t_f)}{k_m}\left[\frac{k_m+(1-k_m-\mathbb{R})F}{k_m}\right]^{\frac{k_m-1}{1-k_m-\mathbb{R}}}, \tag{9a}$$

$$t_f = \frac{\phi_0 z}{(1-k_m-\mathbb{R})F_{\max}} + \frac{k_m[(1-k_m-\mathbb{R})F_{\max}-\phi_0]}{[(1-k_m-\mathbb{R})F_{\max}]^2}\ln\left[\frac{k_m+(1-k_m-\mathbb{R})F}{k_m}\right], \tag{9b}$$

where t_f is the time needed for the trace element to travel from the base to its current position (z or F) in the melting column. The function notation $C_s^0(t-t_f)$ means: given the functional form $C_s^0(t)$ of variable t, $C_s^0(t-t_f)$ is obtained by replacing the original variable t by the new variable $t-t_f$.

The time-dependent batch melting model is obtained by setting the melt suction rate $\mathbb{R} = 0$ in Eqs. (9a) and (9b):

$$C_f^m(z,t) = \frac{C_s^0(t-t_f)}{k_m+(1-k_m)F}, \tag{10a}$$

$$t_f = \frac{\phi_0 z}{(1-k_m)F_{\max}} + \frac{k_m[(1-k_m)F_{\max}-\phi_0]}{[(1-k_m)F_{\max}]^2}\ln\left[\frac{k_m+(1-k_m)F}{k_m}\right]. \tag{10b}$$

During perfect fractional melting, all the melt generated in residual solid is extracted, hence $\phi_0 = 0$ and $\mathbb{R} = 1$. From Eqs. (9a) and (9b), we have the time-dependent perfect fractional melting model:

$$C_f^m(z,t) = \frac{C_s^0(t-t_f)}{k_m}(1-F)^{\frac{1-k_m}{k_m}}, \tag{11a}$$

$$t_f = -\frac{1}{F_{\max}}\ln(1-F). \tag{11b}$$

Eqs. (9)–(11) are valid for $t > 1$. These equations recover the familiar double-porosity melting model of Iwamori (1994), the batch melting model of Ribe (1985b), and the perfect fractional melting model when composition of the incoming solid at the base of the

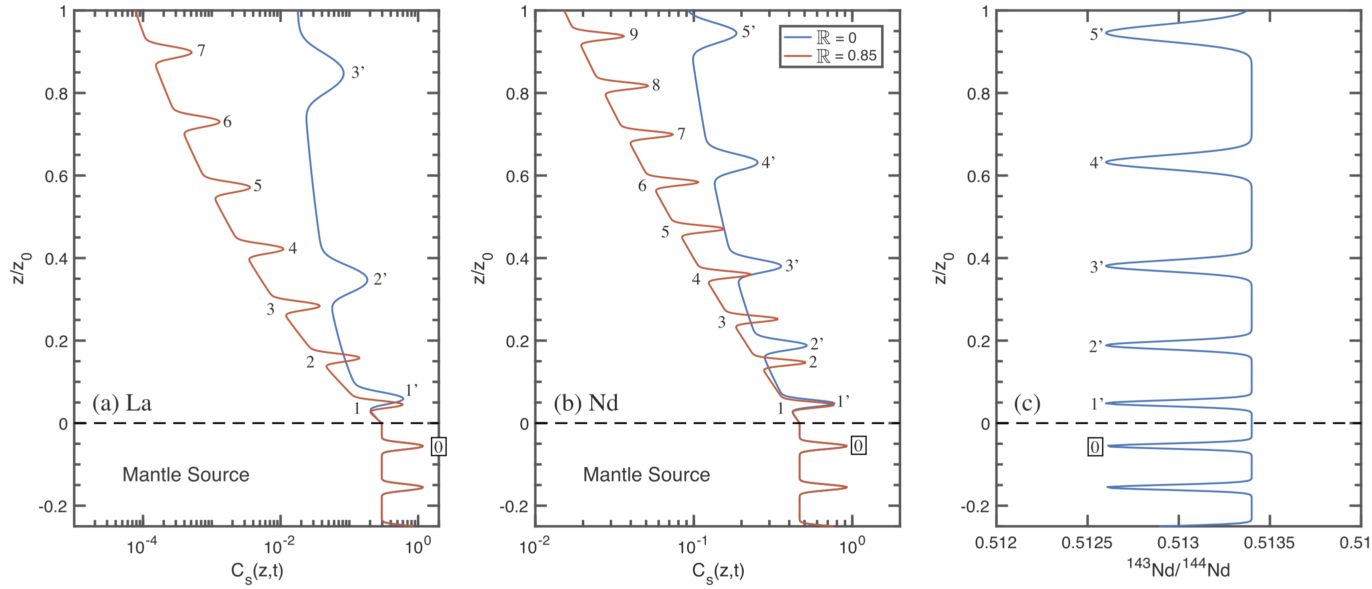

Fig. 3. Distributions of La and Nd in the solid matrix for two choices of melt suction rate (panels a and b). For comparison Nd isotope ratio for the case of batch melting is shown in (c). The dashed lines mark the mantle solidus. La and Nd bulk partition coefficients (0.009 and 0.034) and their abundances in DM (0.296 and 0.465, normalized to primitive mantle) are from Workman and Hart (2005). Abundances of EM are twice those of DM. The maximum extent of melting at the top of the melting column is 15%. Porosities at the top of the melting column are 1.9% for the case of batch melting and 0.92% for the case of $\mathbb{R} = 0.85$. These values correspond to a reference porosity of 2% (Fig. 2a). (For interpretation of the colours in the figure, the reader is referred to the web version of this article.)

melting column is independent of time. Hence Eqs. (9a) and (9b) represent a general time-dependent model for melting a chemically heterogeneous mantle. Given the matrix melt composition, the abundance of a trace element in residual solid (C_s^m) can be calculated using the solid–melt partition coefficient k_m. Examples calculated using Eqs. (9) and (10) and related discussions will be presented in the next section. Expressions for the concentration of an incompatible trace element in the channel melt are given in Appendix B (Eqs. (B.7)–(B.9)). Expressions for a case of linear melting rate ($F = F_{\max} z^2$) are presented in Appendix C.

3. Essential features of time-dependent melting

The functional form of the time-dependent melting model (Eq. (9a)) is the same as the steady-state melting model (Eq. (2)), except the source composition in the former can vary as a function of time and spatial coordinate. In terms of trace element fractionation in the matrix, the steady-state and time-dependent melting models give exactly the same result for a given source composition. If the solid–melt partition coefficient k_m is mass independent for the isotopes of a trace element, melting will not fractionate isotope ratios of the element, as the melting function (terms in the square bracket on the right hand side of Eq. (9a)) is cancelled out when taking the ratio. Isotope ratio of the matrix solid (R) is identical to that of the interstitial melt, and is related to its initial value in the mantle source through the nonlinear mapping:

$$R(z,t) = R_0(t - t_f), \tag{12}$$

where t_f is a function of spatial coordinate z, given by Eq. (9b). The time-dependent model, therefore, can be used to keep track the melting history (i.e., F, z, and t) of a parcel of mantle source marked by trace elements and isotope ratios in melting column. Eqs. (9) and (12) are well suited for studying the fate of chemically heterogeneous sources during melting and melt migration in an upwelling mantle.

3.1. An illustrated example of time-dependent melting

The size and distribution of chemical heterogeneities in the mantle are not known. To highlight the essential features of the time-depending batch and fractional melting models, we consider melting history of a two-component mantle in which the enriched mantle (designated as EM) is embedded in the depleted background mantle (DM). For purpose of illustration, we use linear combinations of Gaussian functions to describe the size and shape of the heterogeneous source that feeds into the melting column at time t in the examples below, viz.,

$$C_s^0(t) = C_{DM}^0 + \left(C_{EM}^0 - C_{DM}^0\right)\sum_{j=1}^{M}\exp\left[-\left(\frac{t-t_j}{b_j}\right)^2\right], \tag{13}$$

where C_{DM}^0 and C_{EM}^0 are concentrations of a trace element in the background and enriched mantle sources, respective; t_j is the time when the center of Gaussian peak j is at the bottom of the melting column ($z = 0$); b_j is a parameter describing the width of Gaussian-shaped heterogeneity; and M is the total number of the enriched sources.

Figs. 3a–3c present a snap shot of compositional variations of La, Nd, and ^{143}Nd/^{144}Nd ratio in the residual solid matrix in the upwelling column for two choices of melt suction rate. To facilitate comparison, we consider a train of Gaussian-shaped enriched mantle that are initially identical in size and evenly spaced in the background mantle (peak-to-peak separation distance of 0.1 dimensionless units, regions below the dashed lines in Fig. 3). Since we scaled time by solid upwelling velocity, adjacent peaks in Figs. 3a–3c are separated from each other by 0.1 time units, i.e., if peak 9 in Fig. 3b entered the melting column at $t = 2.1$, peaks $8, 7, \ldots, 1$ crossed the solidus ($z = 0$) at $t = 2.2, 2.3, \ldots, 2.9$, respectively. Since the initial sizes of the enriched mantle are the same in this example, Figs. 3a–3c can also be used to illustrate temporal evolution of a specific enriched source (e.g., peak 0). A movie showing the spatial and temporal evolution of the solid compositions in the melting column for times between 2 and

3.2 units can be found in supplementary materials (Movie_1.mp4). Two important observations can be readily made from Figs. 3a–3c and the accompanying animation.

Similar to the time-dependent dynamic melting model, solutions for the 1D time-dependent double-porosity model are superposition of a train of enriched pockets traveling along concentration profiles established by steady-state solutions for the background mantle (DM). This is a common feature for melting a spatially distributed and chemically heterogeneous mantle. With the exception of perfect fractional melting where there is no melt left in the matrix, chromatographic fractionation is present in all other cases. The chromatographic effect is stronger for greater melt flux or near batch melting (cf. blues and red curves in Figs. 3a–3c) than near fractional melting (cf. La and Nd peaks marked by the same number, such as 3 or 3′). Unlike the dynamic melting model which has a constant effective velocity (Eq. (3)), the upward increase in the melt flux (Fig. 2b) results in accelerated separation of La from Nd in the upper part of the melting column (e.g., from pocket 1′ to pockets 2′ and 3′).

In contrast to the time-dependent dynamic melting model, the relative size and shape of the enriched blob change spatially and systematically in the matrix solid and melt. This is highlighted by the case of batch melting ($\mathbb{R} = 0$, blues curves in Figs. 3a–3c). Starting below the solidus, the enriched pocket 0 would evolve to pockets 1′, 2′, 3′, 4′, and 5′ after time increments of 0.1, 0.2, 0.3, 0.4, and 0.5 units, respectively. Hence the size of the enriched source is significantly increased by the upward acceleration of the percolating melt. At a given time, the amount of stretching for La is greater than that for Nd (cf. pockets labeled 3′ in Figs. 3a–3c). For a given trace element, the amount of stretching depends strongly on the style of melting (i.e., fractional vs. batch): the greater the extent of melt extraction (i.e., the larger the $\mathbb{R}$), the smaller the amount of stretching will be. Because solid velocity decreases upward due to melting and melt extraction, the size of a chemical heterogeneity is actually shrunk for the case of perfect fractional melting. We will quantify the stretching effect in the next section.

3.2. Stretching factor for the matrix

The amount of stretching or deformation experienced by a mantle parcel depends on the bulk solid–melt partition coefficient and the melt suction rate, and can be estimated using the effective transport velocity (Eq. (5)). Consider a thin layer of chemical heterogeneity of initial thickness h_0 at the onset of melting. The time it takes for the layer to pass through the solidus at the bottom of the melting column is

$$t^* = \frac{h_0}{V_s^0}. \tag{14}$$

Since the time it takes for a mantle parcel or melt to pass through the steady-state melting column is constant, by the time the bottom of the enriched layer exits the top of the melting column, the top of the enriched layer would have moved ahead by the amount or distance that equals to the stretched length or thickness of the enriched layer, viz.,

$$\begin{aligned} h^m_{stretched} &= V_{eff}t^* \\ &= \frac{\rho_s V_s^0[(1-\mathbb{R})F_{\max} + (1-F_{\max})k_m]}{\rho_f\phi_m + \rho_s(1-\phi_m)k_m}\,\frac{h_0}{V_s^0}. \end{aligned} \tag{15}$$

Hence the relative amount of stretching experienced by the enriched layer at the top of the melting column, termed the stretching factor hereafter, is given by the simple expression:

$$\frac{h^m_{stretched}}{h_0} = \frac{\rho_s[k_m + (1-k_m-\mathbb{R})F_{\max}]}{\rho_f\phi_m + \rho_s(1-\phi_m)k_m}, \tag{16a}$$

where ϕ_m and k_m are evaluated at the top of the melting column. Equation (16a) is valid so long as the thickness of the enriched layer is much smaller than the height of the melting column.

The porosity at the top of the melting column can be calculated using the simple expression:

$$\phi_m \approx \phi_{ref}\left[(1-\mathbb{R})\right]^{\frac{1}{n}}, \tag{16b}$$

where n is the exponent in the permeability-porosity relation (Eq. (A.3)); ϕ_{ref} is a reference or characteristic porosity of the matrix defined by Eq. (A.5) in Appendix A. The value of ϕ_{ref} is within a few percent of the porosity of the matrix for batch melting (cf. Fig. 2a). In general, the larger the matrix permeability, the greater the efficiency of melt percolation and the smaller the reference porosity will be. Fig. 2a presents an example of calculated porosity in the melting column for a case of $\phi_{ref} = 0.02$ and several choices of the melt suction rate (a similar plot for the case of $\phi_{ref} = 0.04$ is given in supplementary Fig. S1). For near fractional melting ($\mathbb{R} = 0.8 \sim 0.95$), matrix porosities at the top of the melting column are in the range 0.5%∼1% when $\phi_{ref} = 0.02$ and 0.7%∼1.8% when $\phi_{ref} = 0.04$.

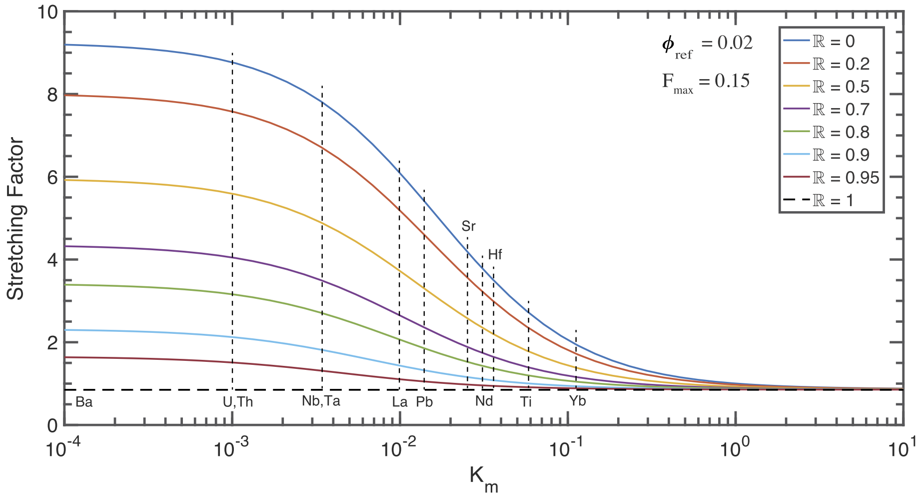

Fig. 4. Variations of stretching factor as a function of bulk solid–melt partition coefficient for selected melt suction rates. The case of perfect fractional melting is shown as the dashed horizontal line. Vertical dashed lines are used to mark selected trace elements and to facilitate discussion. The extent of melting at the top of the melting column is 15%. The reference porosity is 2%. (For interpretation of the colours in the figure, the reader is referred to the web version of this article.)

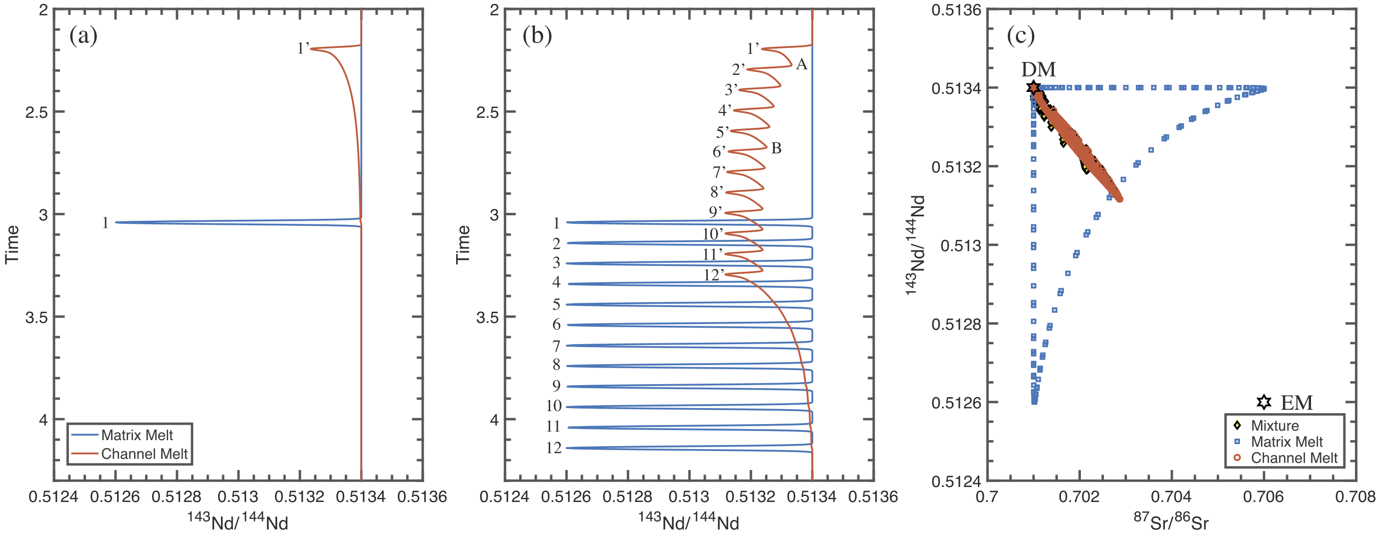

Fig. 5. Variations of Nd and Sr isotope ratios in the matrix melt and the channel melt emerging at the top of the melting column. (a) Case of a single Gaussian-shaped heterogeneity. (b) A train of 12 identical Gaussian-shaped heterogeneities. (c) Correlations between Sr and Nd isotope ratios. Composition of the mixture in panel c is a weighted average (melt flux) between the channel melt and the matrix melt. The bulk partition coefficient for Sr in the matrix used in the model calculation is 0.025. Other parameters are the same as those used for Nd in the case of $\mathbb{R} = 0.85$ in Fig. 3b. To facilitate description, the labeling of the enriched pockets is reversed compared to the case shown in Fig. 3b. (For interpretation of the colours in the figure, the reader is referred to the web version of this article.)

Fig. 4 displays variations of stretching factor as a function of bulk solid–melt partition coefficient for a range of melt suction rate. When $k_m \ll \phi_m$, which is likely the case for highly incompatible trace elements during peridotite melting, the stretching factor is insensitive to partition coefficient. From Eq. (16), we have

$$\frac{h^m_{stretched}}{h_0} \rightarrow \frac{(1-\mathbb{R})F_{\max}}{\phi_m}. \tag{17}$$

For 1% porosity and 15% melting at the top of the melting column, the stretching factor is 3 for $\mathbb{R} = 0.8$ and 1.5 for $\mathbb{R} = 0.9$. From highly to moderately incompatible trace elements, Fig. 4 shows that the stretching factor decreases systematically along the curve of constant melt suction rate. For near batch melting (e.g., $\mathbb{R} \leq 0.2$), the stretching factors are 7.5–8.7 for U and Th, 4.6–5.4 for Pb, 3.5–4.2 for Sr, 3.4–4 for Nd, and 3–3.5 for Hf. For near fractional melting ($\mathbb{R} = 0.8 \sim 0.95$), the stretching factors are 1.5–3.1 for U and Th, 1–1.8 for Pb, 0.98–1.5 for Sr, 0.96–1.4 for Nd, and 0.95–1.38 for Hf. For Sr, Nd, and Hf, their stretching factors are reduced by approximately 30% for the reference porosity of 4% compared to the case shown in Fig. 4.

When the trace element is considerably compatible (i.e., $k_m > 2$), the stretching factor is insensitive to both k_m and ϕ_m, and approaches the asymptotic value for perfect fractional melting:

$$\frac{h^m_{stretched}}{h_0} \rightarrow 1 - F_{\max}. \tag{18}$$

This is illustrated in Fig. 4 for the maximum extent of melting of 15%. The stretching factor in this case is 0.85, i.e., the heterogeneity is shrunk in size for the compatible elements during its transit in the melting column.

3.3. Melt compositions at the top of the melting column

Here we use the example of near fractional melting shown in Fig. 3b (case $\mathbb{R} = 0.85$) to illustrate how compositions of the melt emerging at the top of the melting column vary as a function of time during melting a two-component mantle that consists of a train of 12 identical Gaussian-shaped EM in the background DM (Eq. (13)). Figs. 5a and 5b display Nd isotope ratios in the matrix melt and the channel melt at the top of the melting column. The enriched Gaussian peak 1 entered the melting column at $t = 2.1$. This peak exited the top of the melting column at $t = 2.196$ through the dunite channel, but at $t = 3.042$ through the residual matrix (Fig. 5a). If the solid upwelling time (t_0) is 1 Myr, it takes 96 kyr for the enriched signal to pass through the high-porosity dunite channel, but 942 kyr to sail through the low-porosity matrix. (For $\mathbb{R} = 0.95$, it takes 86 kyr and 1.15 Myr for the enriched signal to pass through the channel and the matrix, respectively.) In the time domain, the shape of the enriched signal in the mantle source is preserved in the matrix melt collected at the top of the melting column but its size is stretched (cf. Fig. 3c for $z < 0$). However, the enriched signal is diluted in the channel by addition of depleted melts sucked from the matrix to the channel in the melting column. As the fast moving depleted channel melt passing by the slow moving enriched residual layer in the melting column from below, it is contaminated by the enriched melt sucked from the matrix, producing the long trailing tail in the channel melt (region between points 1 and 1′ in Fig. 5a). When there are two or more EM pockets in the melting column, such as the ones shown in Figs. 3b and 5b, the contamination is additive. For example, the more enriched peak 5′ in the channel melt results from superposition of channel melt derived from Gaussian peak 5 in the matrix and part of the tails from peaks 1′, 2′, 3′, and 4′ in the channel (segment A–B in Fig. 5b). This explains the systematic rise in the enriched signals from peaks 1′ to 9′ in Fig. 5b. A movie illustrating the various effects is provided in the supplementary materials (Movie_2.mp4).

Because of its higher velocity, channel melt samples existing heterogeneities in the melting column on its way to the top. Composition of the channel melt at the top of the melting column is a weighted average of all the melts in the channel (Eq. (B.8a) in Appendix B). Therefore, variations in isotope and chemical compositions of the channel melt are generally smaller than those in the matrix melt and residue solid for melting a heterogeneous mantle source. This is illustrated in the Sr–Nd isotope variation diagram in Fig. 5c. Here the correlation between Sr and Nd isotope ratios and their reduced ranges of variation in the channel melts are due to a combined effect of melt migration induced mixing and the highly incompatible nature of Sr and Nd in the dunite channel. The anti-correlation between Sr and Nd isotope ratios in matrix melts is due to the chromatographic effect. However, the latter

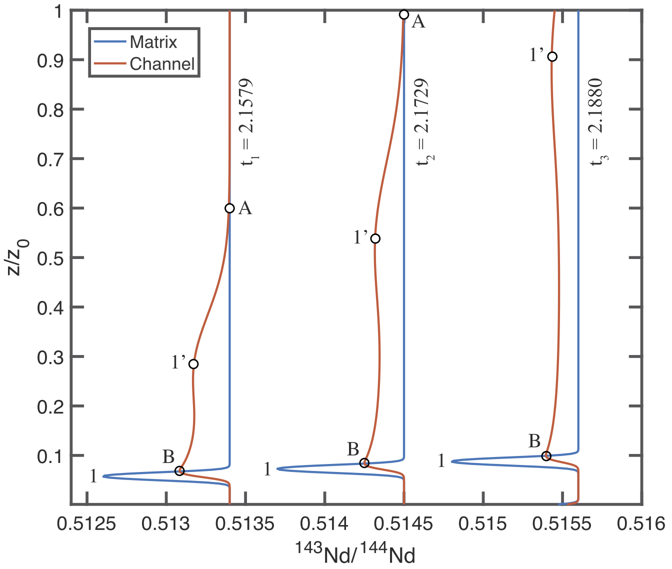

Fig. 6. Variations of Nd isotope ratio in the matrix melt and the channel melt in the melting column at three times. The enriched peaks 1 and 1′ entered the melting column at $t = 2.1$. For diagram clarity, results for t_2 and t_3 are shifted to the right by 0.0011 and 0.0022 units, respectively. Parameters are the same as those used for Nd in the case of $\mathbb{R} = 0.85$ in Fig. 3b. (For interpretation of the colours in the figure, the reader is referred to the web version of this article.)

effect is nearly wiped out by mechanic mixing between the matrix melt and the channel melt at the top of the melting column (diamonds in Fig. 5c) because the channel melt flux is considerably larger than the matrix melt flux in the present case of near fractional melting. Correlations such as the one shown in Fig. 5c have been widely observed in basalts from mid-ocean ridges and ocean islands. To interpret the isotope data in the framework outlined here, one also needs to consider the geometry or shape of the melting region and mixing processes in the magma conduit and magma chamber. In Liu and Liang (2017b), we showed how these additional constraints could be integrated into a pseudo-2D double-porosity model for melting a two-component mantle beneath mid-ocean ridge spreading centers.

3.4. Stretching chemical heterogeneities by melt migration in high-porosity dunite channels

Once extracted to high-porosity channels, a pocket of chemical heterogeneity will be further stretched during its ascent through the channel network. The stretching, however, is asymmetric with respect to the frontside and backside of the heterogeneity or wave pocket. As shown in Fig. 6 and supplementary Movie_2.mp4, the frontside of the wave (segment 1′-A) is stretched in response to upward acceleration of the channel melt, while the backside of the wave (segment B-1′) is continuously stretched as the trailing and depleted channel melt passes by the enriched layer in the melting column (i.e., the contamination effect discussed in Section 3.3). For an incompatible trace element in dunite channels, the frontside of the enriched signal is stretched by a factor of 30 for near fractional melting (Eq. (B.10) in Appendix B). Hence the enriched signal in the channel melt is quickly spread over part of the melting column above the enriched layer in the solid matrix while its amplitude is damped significantly (regions above point B in Fig. 6). If the volume fraction of EM is small relative to the background DM, the channel melt will not be able to sample the endmember EM component (Fig. 5c). This provides a simple explanation to the observed Nd isotope difference between MORB and their spatially associated abyssal peridotites (Liu and Liang, 2017b): the former preferentially sample the channel melts (Kelemen et al., 1997), whereas the latter can sample both the depleted and enriched mantle components, although the process is complicated by disequilibrium chemical exchange in the matrix (see Section 5.1 below).

4. Discussion

4.1. Batch melting followed by near fractional melting

The preceding section demonstrates the importance of the style of melt migration in determining the extent of chemical deformation recorded by trace elements or their isotope ratios in a pocket of enriched mantle. Strong stretching is observed for most geochemically important incompatible trace elements during batch or near batch melting, whereas a factor of two or less amount of stretching is possible for chemical heterogeneities marked by radiogenic isotopes U, Th, Pb, Sr, Nd and Hf during near fractional melting (Fig. 4). Although the very depleted nature of LREE in clinopyroxenes in abyssal peridotites is suggestive of near fractional melting (Johnson et al., 1990; Johnson and Dick, 1992; Hellebrand et al., 2002; Brunelli et al., 2006; Warren, 2016), it has been demonstrated that the same REE patterns in residual clinopyroxenes can also be explained by a combination of batch melting and near fractional melting (Kelemen et al., 1997; Asimow, 1999; Liang and Peng, 2010). The combination of batching melting in the lower part of the melting column followed by near fractional melting in the upper part of the melting column is physically more realistic as the driving force for pyroxene dissolution is relatively small near the mantle solidus, making it difficult to initiate high-porosity channels at depth greater than multiple saturation depth in the mantle (Kelemen, 1990; Beck et al., 2006; Lambart et al., 2009).

Including batch melting in the lower part of the upwelling column (for $F < F_d$), the mass flux of the matrix melt in the upper part of melting column becomes (Liang and Peng, 2010),

$$\rho_f \phi_m V_f^m = \rho_s V_s^0 \big[F_d + (1 - \mathbb{R})(F - F_d) \big], \quad \text{for } F \geq F_d. \tag{19a}$$

The stretching factor in Eq. (16a) then takes on the more general expression:

$$\frac{h^m_{stretched}}{h_0} = \frac{\rho_s [k_m + \mathbb{R} F_d + (1 - k_m - \mathbb{R}) F_{\max}]}{\rho_f \phi_m + \rho_s (1 - \phi_m) k_m}, \quad \text{for } F_{\max} \geq F_d. \tag{19b}$$

Hence at the onset of channelization ($F = F_d$), a chemical heterogeneity may have already been stretched considerably by melt migration. This is illustrated in Fig. 7 for a case of near fractional melting in the upper part of the melting column ($\mathbb{R} = 0.9$, $F_{\max} = 0.15$, $\phi_{ref} = 0.02$, and several choices of F_d). For 5% batch melting in the lower part and 10% near fractional melting in the upper part of the melting column, Fig. 7 shows that heterogeneities recorded by radiogenic isotopes U, Th, Pb Sr, Nd and Hf are stretched by at least a factor of 2 at the top of the melting column. Hence stretching of chemical heterogeneity in residual peridotites is inevitable during decompression melting and channelized melt extraction.

4.2. Stretching and deforming chemical heterogeneity by melt migration in 2D and 3D

Stretching chemical heterogeneity by melt migration in higher dimensions will result in changes in geometric shape of the mantle source heterogeneity. This can be illustrated using a simplified 2D time-dependent model in which all the physical parameters (melt and solid velocities, degree of melting, melting and melt suction rates) are independent of horizontal coordinate (x), i.e., the flow

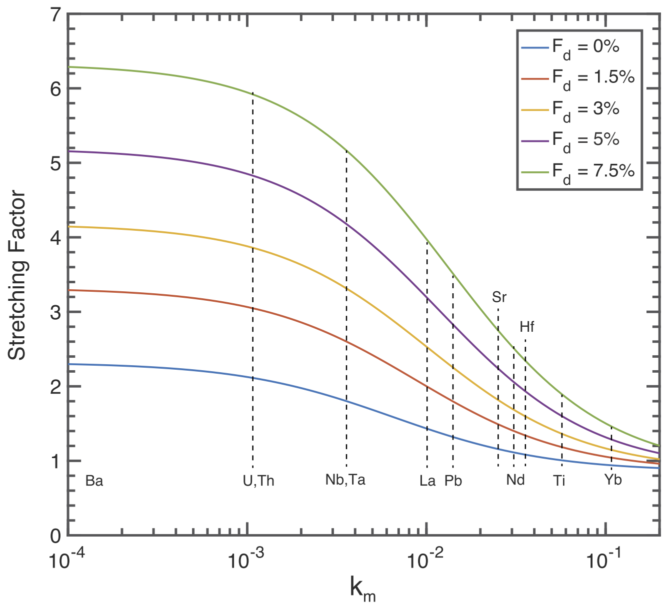

Fig. 7. Variations of stretching factor as a function of bulk solid–melt partition coefficient for a case of near fractional melting in the upper part of the melting column ($\mathbb{R} = 0.9$) and batch melting in the lower part of the melting column with 5 choices of Fd. Vertical dashed lines are used to mark selected trace elements and to facilitate discussion. The extent of melting at the top of the melting column is 15%. The reference porosity is 2%. (For interpretation of the colours in the figure, the reader is referred to the web version of this article.)

fields are effectively 1D along the vertical direction. The mantle source composition varies both vertically and horizontally (Fig. 1). The boundary condition at the base of the melting column ($z = 0$) for a trace element or isotope ratio depends on time and horizontal coordinate, viz.,

$$C_s(x, 0, t) = C_s^0(x, t), \qquad R(x, 0, t) = R_0(x, t). \tag{20a}$$

Solutions for a trace element and isotope ratio in residual solid matrix take on the forms:

$$C_s^m(x, z, t) = C_s^0(x, t - t_f)\left[\frac{k_m + (1 - k_m - \mathbb{R})F}{k_m}\right]^{\frac{k_m - 1}{1 - k_m - \mathbb{R}}}, \tag{20b}$$

$$R(x, z, t) = R_0(x, t - t_f), \tag{20c}$$

where t_f is the same as that given by Eq. (9b). This 2D model (Eqs. (20a)–(20c)) can be readily generalized to 3D.

Fig. 8 presents two examples of melt migration induced shape change or chemical deformation in 2D melting columns in which the solid and melt flow directions are vertical, one for batch melting ($\mathbb{R} = 0$) and the other for near fractional melting ($\mathbb{R} = 0.85$). A movie showing the spatial and temporal evolution of the two enriched regions marked by contours of constant ^{143}Nd/^{144}Nd isotope ratio can be found in supplementary materials (Movie_3.mp4). Vertical stretching due to melt flow has significantly changed the original shape of the enriched regions in the mantle source (dashed contours in Fig. 8). By the time the top of the enriched regions arrive at the top of the melting column, the areas of the enriched region are increased by factors of approximately 3.91 and 1.26, respectively, for the batch melting and near fractional melting examples shown in Figs. 8a and 8b. In more general settings such as corner flow around ridge axis, streamlines of the melt and solid flow fields diverge from each other (e.g., Spiegelman, 1996). Blobs of enriched mantle will be further stretched and deformed.

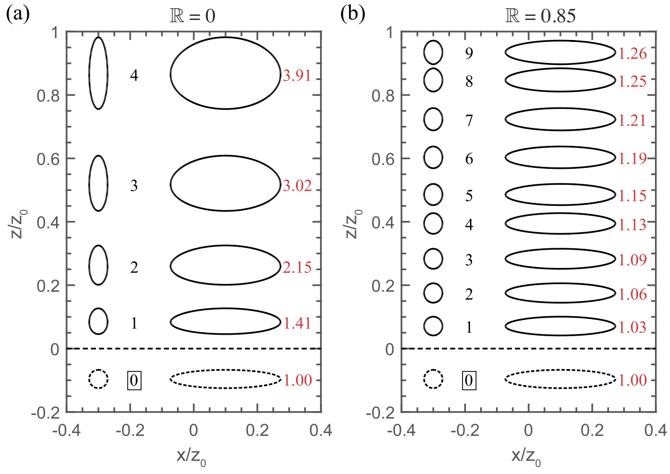

Fig. 8. Changing shapes of chemical heterogeneity during batch melting (a) and near fractional melting (b) in 2D upwelling columns. Two enriched regions are enclosed by a contour of constant ^{143}Nd/^{144}Nd isotope ratio. The enriched mantle sources are enclosed by the dashed circle and ellipsis below the solidus ($z < 0$). Melting parameters are the same as those used in Fig. 3.

5. Summary and further discussion

5.1. Assumptions, simplifications, and limitations

To focus on essential features of the time-dependent batch melting and fractional melting models while keeping the problem simple, we limited our presentation and discussion on modal melting. During adiabatic mantle melting, clinopyroxene and orthopyroxene modal abundances decrease upward, and depending on melting reactions, clinopyroxene is completely consumed by 18 ∼ 22% of melting of DMM (Walter, 2003). Hence bulk solid–melt partition coefficients for incompatible trace elements decrease upward along the melting column. For example, bulk partition coefficients of La and Nd decrease from 0.01–0.004 and 0.031–0.016, respectively, for 0 ∼ 15% of melting of a spinel lherzolite. The stretching factors shown in Figs. 4 and 7 would further increase for non-modal melting. Solutions for non-modal melting are presented in Appendix B.

A key simplification used in the present study and most geochemical investigations of mantle melting is the assumption of local chemical equilibrium between the solid and the interstitial melt in the matrix. Inverse modeling of REE depletion in clinopyroxenes in abyssal peridotites demonstrated the need of a small extent of chemical disequilibrium to account for the less fractionated LREE patterns in a large fraction of residual peridotite samples from Mid-Atlantic Ridge, Central Indian Ridge, Southwest Indian Ridge, Lena Trough, and American–Antarctic Ridge (101 out of 135 samples, Liang and Liu, 2016; Liu and Liang, 2017a). A finite solid–melt exchange rate due to slow cation diffusion in clinopyroxene reduces the extent of depletion of incompatible trace elements in residual solid, increasing the effective solid–melt partition coefficient (Qin, 1992; Iwamori, 1994; Van Orman et al., 2002; Liang and Liu, 2016). Hence for slow diffusing cations, such as LREE and Hf, their stretching factors will be less than those predicted by the equilibrium melting models. In a case of equilibrium batch melting in the lower part of the melting column and disequilibrium near-fractional melting in the upper part of the melting column, the extent of stretching due to a finite solid–melt exchange rate is likely to be small to negligible, as most of the stretching takes place during batch melting (Fig. 7).

The lack of instantaneous local chemical equilibrium between residual solid and interstitial melt in the matrix will result in smearing or spreading of an enriched signal when the enriched matrix melt moves ahead of the enriched solid (Liu and Liang, 2017b). Spreading of the enriched front depends on the difference between melt and solid velocities, solid–melt chemical exchange rate, as well as solid–melt partition coefficient. Overall, a blob of chemical heterogeneity will be further deformed during disequilibrium melt migration in the upwelling mantle. This dispersion effect, which is especially significant in the presence of 2D and 3D flow fields, will be quantified in a follow-up study.

To obtain simple analytical solutions to the time-dependent melting problems, we approximate the matrix porosity in the time derivative of the mass conservation equations (Eqs. (6) and (8a)) as a linear function of the vertical coordinate. Use of a power-law relationship for the matrix porosity (e.g., $\phi_m \propto z^{1/2}$) makes the algebra more tedious but will not change the basic features of the time-dependent melting nor the conclusions based on our simplified models. In fact, expressions for the stretching factors (Eqs. (16a), (19b), and (B.10)) are independent of the linear approximation.

To demonstrate the basic idea of stretching while keeping the problem tractable, we considered a case of constant melting rate (Eq. (8c)). During decompression melting of mantle peridotite, the melt productivity or melting rate increases upward until clinopyroxene is exhausted in the melting column (e.g., Asimow et al., 1997). Since the stretching factor depends explicitly on $F_{\max}$ (Eq. (16a)), the total amount of stretching at the top of the melting column is not sensitive to particular choice of the melting rate. For a given $F_{\max}$, upward increase in the matrix melting rate results in smaller melt flux in the lower part of the melting column and higher melt flux, hence greater acceleration, in the upper part of the melting column compared to the case of constant melting rate. Consequently, a pocket of chemical heterogeneity is less stretched in the lower part, but more stretched in the upper part, of the melting column compared to the case of constant melting rate. These effects are illustrated in supplementary Figs. S3 and S4 and animation Movie_4.mp4, calculated using the analytical solution for modal melting with a linear melting rate (Eqs. (C.2a)–(C.2b) in Appendix C).

In the upper most part of the upwelling mantle column beneath a mid-ocean ridge spreading center where clinopyroxene is exhausted by melting (e.g., Asimow et al., 1997), the matrix melting rate may be considerably smaller than the matrix dissolution rate. Compaction-dissolution waves may arise, which will further distort the size and shape of chemical heterogeneities in the matrix, complicating the interpretation of geochemical data based on models presented here (Hesse et al., 2011; Liang et al., 2011).

And finally, as a first study of time-dependent batch and fractional melting, we limited our analysis to melting a chemically heterogeneous mantle column that has a homogeneous lithology at the onset of partial melting. The latter assumption allows us to set the mechanic properties (e.g., porosity and velocity) of the melting column to steady state. For melting a lithologically heterogeneous mantle, such as blobs of pyroxenite imbedded in a lherzolite matrix, the problem is considerably more complicated: (1) the mechanic properties are likely time-dependent as porosity waves may arise due to differences in melting rate and permeability among various lithologies in the melting column (e.g., Barcilon and Richter, 1986); and (2) melts derived from the imbedded blobs may react with the overlying peridotitic matrix (e.g., Yaxley and Green, 1998), producing new lithologies that have different partition coefficients and melting reactions. These complicated but more realistic processes are still not well understood and hence difficult to quantify in geochemical modeling (but see Watson and Spiegelman, 1994; Jordan et al., 2018), but may result in further stretching and spreading of an enriched isotope or incompatible trace element signal during melt migration in the heterogeneous mantle. Melting a lithologically heterogeneous mantle is an important topic and requires detailed studies.

5.2. Conclusions

During decompression melting, the melt and solid mass fluxes and porosity vary spatially in the melting column. This is a key difference between the present melting models and the dynamic melting model. Although this difference is not crucial in assessing the depletion of incompatible trace elements during partial melting, it is important in determining the size and shape of a chemical heterogeneity in the upwelling melting column. The present study helps to establish a theoretical framework for studying spatially and temporally correlated mantle and mantle-derived samples. The main conclusions of this study can be summarized as follows:

1. In terms of mathematic expression, the time-dependent batch melting (Eq. (10a)), dynamic melting (Liang, 2008), and fractional melting models (Eqs. (9a), (11a) and (20b)) share a common feature: the matrix melt or solid composition is a product of model specific melting function and time-dependent mantle source composition. Since melting alone cannot fractionate isotopes of heavy elements, isotope ratios of trace elements are advected through the upwelling melting column at their effective transport velocities (Eq. (5)) while their values remain unchanged in the matrix melt and solid.
2. During decompression melting, the matrix melt mass flux increases while the matrix solid mass flux decreases upward, resulting in an acceleration of the effective transport velocity for an incompatible trace element in the matrix. Consequently, a blob of chemical heterogeneity will be stretched during its transit through the melting column. The amount of stretching is sensitive to bulk solid–melt partition coefficient and the style of melting and melt extraction. For radiogenic isotopes U, Th, Pb, Sr, Nd, and Hf in the matrix, a factor of 4 ∼ 8 stretching is expected for batch melting, but considerably smaller extent of stretching is predicted for near fractional melting (Fig. 4). If batch melting takes place in the lower part of the melting column, a factor of two or more stretching can be expected for the radiogenic isotopes in a peridotitic matrix (Fig. 5).
3. Melt migration in higher dimensions (2D and 3D) will change the shape of mantle source heterogeneity, introducing additional complexity to the interpretation of geochemical data of basalts and residual peridotites. This higher dimension effect is especially significant when the flow field of the melt is different from that of the solid.
4. During near fractional melting, the channel melt flux increases considerably toward the top of the melting column. The enriched signal in the channel melt is stretched from the location of its source in the solid matrix to the top of the melting column while its amplitude is damped significantly. The channel melt emerging at the top of the melting column is a weighted average of all the melts (i.e., both enriched and depleted) in the melting column. Chemical heterogeneities observed in peridotite matrix and dunite channel therefore are decoupled both spatially and temporally.
5. Superposition of channel melt is an important consequence of melt migration induced mixing in a chemically heterogeneous melting column and needs to be considered when interpreting time-series geochemical data, such as radiogenic isotope ratios in basalts from a given locality.
6. Finally, in the presence of chemical disequilibrium, a chemical heterogeneity can be further stretched by smearing or dispersion during melt migration in the matrix. This disequilibrium effect is potentially important for melt migration in 2D and 3D settings and requires further investigation.

Acknowledgements

This paper benefited from thoughtful reviews by Jacob Jordan and two anonymous reviewers. This work was supported by National Science Foundation grants EAR-0911501 and EAR-1624516.

Appendix A. Porosity in the melting column

For simplicity, we use Darcy's law to estimate the steady-state melt porosity in the matrix (McKenzie, 1984):

$$\phi_m\left(V_f^m - V_s^m\right) = \frac{\kappa_\phi}{\eta_f}(1-\phi_m)\Delta\rho g, \tag{A.1}$$

where κ_ϕ is the matrix permeability; η_f is the melt viscosity; $\Delta\rho = \rho_s - \rho_f$; and g is the acceleration due to gravity. With the help of Eqs. (4a) and (4b), we can write the relative melt flux in Eq. (A.1) as

$$\phi_m\left(V_f^m - V_s^m\right) = V_s^0\left[(1-\mathbb{R})F - \phi_m(1-F)\right], \tag{A.2}$$

where we made use of the simplifications: $\phi_m \ll 1$ and $\rho_s/\rho_f \to 1$. The permeability is related to porosity and mean grain size (d) through the power-law relationship:

$$\kappa_\phi = \frac{d^2}{b}\phi_m^n, \tag{A.3}$$

where n is the permeability exponent; and b is a constant. Substituting Eqs. (A.2) and (A.3) into Darcy's law, we have an algebraic equation for the matrix porosity:

$$\phi_m^n = \frac{b\eta_f}{d^2\Delta\rho g}V_s^0\left[(1-\mathbb{R})F - \phi_m(1-F)\right]. \tag{A.4}$$

Given the number of material constants and model parameters in Eq. (A.4), it is convenient to introduce a characteristic or reference porosity in terms of the maximum extent of melting experienced by the melting column:

$$\phi_{ref} = \left(\frac{b\eta_f}{d^2\Delta\rho g}V_s^0 F_{\max}\right)^{\frac{1}{n}}. \tag{A.5}$$

Eq. (A.4) then becomes

$$\phi_m^n = \frac{\phi_{ref}^n}{F_{\max}}\left[(1-\mathbb{R})F - \phi_m(1-F)\right]. \tag{A.6}$$

Given the reference porosity and melting parameters, Eq. (A.6) can be solved "exactly" using a numerical method. An approximate solution to Eq. (A.6) can be obtained by ignoring the second term in the square bracket on the right hand side of this equation, viz.,

$$\phi_m \approx \phi_{ref}\left[(1-\mathbb{R})\frac{F}{F_{\max}}\right]^{\frac{1}{n}}. \tag{A.7}$$

Hence the reference porosity corresponds to a special case of batch melting ($\mathbb{R}=0$) in which contribution from solid upwelling is negligible. The porosity at the top of the melting column is given by

$$\phi_0 \approx \phi_{ref}\left[(1-\mathbb{R})\right]^{\frac{1}{n}}. \tag{A.8}$$

Porosity obtained from the approximate solutions Eqs. (A.7) and (A.8) are slightly smaller than the "exact" values given by Eq. (A.6) (by <5%, relative).

The preceding analysis (Eqs. (A.4)–(A.8)) demonstrates that the matrix porosity depends on the style of melt extraction ($\mathbb{R}$). For near-fractional melting, porosity in the melting column (matrix) can be considerably smaller than that for batch melting (Fig. 1). For perfect fractional melting, $\mathbb{R}=1$, we have $\phi_m = 0$.

Appendix B. Mass Conservation equations

Neglecting diffusion and dispersion in the melts, the 1D mass conservation equation for a trace element in the matrix melt during non-modal melting is (Liang and Peng, 2010),

$$\begin{aligned}&\left[\rho_f\phi_m + \rho_s(1-\phi_m)k_m\right]\frac{\partial C_f^m}{\partial t}\\ &\quad+\left[\rho_f\phi_m V_f^m + \rho_s(1-\phi_m)V_s^m k_m\right]\frac{\partial C_f^m}{\partial z}\\ &\quad=\Gamma_m\left(k_m^p - 1\right)C_f^m,\end{aligned} \tag{B.1}$$

where k_m^p is the solid–melt partition coefficient calculated according to the proportion of minerals participated in the melting reaction. The bulk solid–melt partition coefficient k_m varies along the melting column during non-modal melting and is given by the expression:

$$k_m(z) = \frac{k_m^0 - k_m^p F}{1-F}, \tag{B.2}$$

where k_m^0 is the bulk solid–melt partition coefficient at the onset of melting. The melt and solid mass fluxes in Eq. (B.1) are related to the degree of melting and the extent of melt extraction experienced by the solid matrix via Eqs. (4a) and (4b). Substituting Eq. (B.2) into Eq. (B.1), we have

$$\begin{aligned}&\left[\rho_f\phi_m + \rho_s(1-\phi_m)k_m\right]\frac{\partial C_f^m}{\partial t}\\ &\quad+\rho_s V_s^0\left[k_m^0 + \left(1-k_m^p-\mathbb{R}\right)F\right]\frac{\partial C_f^m}{\partial z} = \Gamma_m\left(k_m^p - 1\right)C_f^m.\end{aligned} \tag{B.3}$$

The effective advection velocity for the trace of interest is

$$V_{eff} = \frac{\rho_s V_s^0\left[k_m^0 + (1-k_m^p-\mathbb{R})F\right]}{\rho_f\phi_m + \rho_s(1-\phi_m)k_m}. \tag{B.4}$$

The bulk partition coefficient k_m in Eqs. (B.3) and (B.4) is given by Eq. (B.2). For a constant source composition, Eq. (B.3) admits steady-state solutions (Iwamori, 1994; Ozawa, 2001; Liang and Peng, 2010).

For variable source compositions, Eq. (B.3) is a time-dependent first order partial differential equation. Given the initial and boundary conditions, it can be solved using the method of characteristics. Similar to the time-dependent dynamic melting problem of Liang (2008), we divide the t–z space into two regions: one for $z > V_{eff}t$ where the original materials in the melting column still remain in part of the melting column; and the other for $z < V_{eff}t$ (or at large times) where all the original materials in the melting column are replaced by new materials upwelled from below. Solution for the domain $z > V_{eff}t$ (or at early times) depends on the initial condition of the column, whereas solution for the domain $z < V_{eff}t$ (or at large times) depends only on the boundary condition at the base of the melting column. Since the large time solution is most relevant to melt migration beneath the mid-ocean ridge, we consider the case $z > V_{eff}t$ in this study.

To proceed, we nondimensionalize Eq. (B.3) by scaling the time and vertical coordinate by the solid upwelling time and the height of column where melting takes place (Eq. (7)). The nondimensionalized equation, after dropping the primes, is

$$\begin{aligned}&\frac{\partial C_f^m}{\partial t} + \frac{(1-F_{\max}z)\left[k_m^0 + (1-k_m^p-\mathbb{R})F\right]}{\phi_0 z + k_m^0 - F_{\max}(\phi_0 z + k_m^p)z}\frac{\partial C_f^m}{\partial z}\\ &\quad= \frac{F_{\max}(1-F_{\max}z)(k_m^p-1)C_f^m}{\phi_0 z + k_m^0 - F_{\max}(\phi_0 z + k_m^p)z}.\end{aligned} \tag{B.5}$$

Solution to the non-modal melting model (Eq. (B.5)) subject to the time-dependent boundary condition Eq. (8d) is

$$C_f^m(z,t) = \frac{C_s^0(t-t_f)}{k_m^0}\left[\frac{k_m^0 + (1-k_m^p-\mathbb{R})F}{k_m^0}\right]^{\frac{k_m^p-1}{1-k_m^p-\mathbb{R}}}, \tag{B.6a}$$

$$\begin{aligned} t_f(z) = {} & \frac{\phi_0 z}{(1-k_m^p-\mathbb{R})F_{\max}} + \frac{k_m^p(1-k_m^p-\mathbb{R})F_{\max} - \phi_0 k_m^0}{[(1-k_m^p-\mathbb{R})F_{\max}]^2} \\ & \times \ln\left[\frac{k_m^0 + (1-k_m^p-\mathbb{R})F}{k_m^0}\right] \\ & + \frac{k_m^0 - k_m^p}{(1+k_m^0-k_m^p-\mathbb{R})F_{\max}} \ln\left[\frac{k_m^0 + (1-k_m^p-\mathbb{R})F}{k_m^0(1-F)}\right]. \end{aligned} \tag{B.6b}$$

Eqs. (B.6a) and (B.6b) recover the Eqs. (9a) and (9b) for modal melting when $k_m^p = k_m^0$.

The concentration of an incompatible trace element in the melt in dunite channels is governed by the mass conservation equation (Liang and Parmentier, 2010):

$$\rho_f \phi_{ch} \frac{\partial C_f^{ch}}{\partial t} + \rho_f \phi_{ch} V_f^{ch} \frac{\partial C_f^{ch}}{\partial z} = \frac{\dot{S}}{\psi}\left(C_f^m - C_f^{ch}\right), \tag{B.7a}$$

where for simplicity, we assume olivine-melt partition coefficients for incompatible trace elements are much smaller than the porosity of the dunite channel. The channel melt flux is the amount of melt sucked from the matrix to the channel adjusted by relative volume proportions of the channel (ψ) and the matrix in the double-porosity column:

$$\rho_f \phi_f^{ch} V_f^{ch} = \frac{1-\psi}{\psi} \rho_s V_s^0 \mathbb{R} F, \tag{B.7b}$$

where the channel porosity is proportional to the reference porosity of the matrix (Eq. (A.5)),

$$\phi_{ch} = \left[\frac{1-\psi}{\psi}\frac{\mathbb{R}F}{F_{\max}}\right]^{\frac{1}{n}} \phi_{ref}. \tag{B.7c}$$

For simplicity, we set the average grain size of the channel the same as that of the matrix in Eq. (B.7c). For $n = 3$, $\psi = 10\%$, and $\mathbb{R} = 0.9$, we have $\phi_{ch} = 2\phi_{ref}$ at the top of the melting column. The channel melt composition is an average of the matrix melt composition, given by the integral:

$$C_f^{ch}(z,t) = \frac{1}{z}\int_0^z C_s^0\left[t - \Theta z^{\frac{1}{n}} + \Theta x^{\frac{1}{n}} - t_f(x)\right] g(x)dx, \tag{B.8a}$$

$$g(x) = \frac{1}{k_m^0}\left[\frac{k_m^0 + (1-k_m^p-\mathbb{R})F_{\max}x}{k_m^0}\right]^{\frac{k_m^p-1}{1-k_m^p-\mathbb{R}}}, \tag{B.8b}$$

$$\Theta = \frac{n\phi_{ref}}{F_{\max}}\left(\frac{1-\psi}{\psi}\mathbb{R}\right)^{\frac{1-n}{n}}, \tag{B.8c}$$

where the time (t) and spatial coordinate (z or x) are scaled by the solid upwelling time and the height of the column where melting takes place; t_f is a function of spatial coordinate (Eq. (B.6b)); and n is the exponent in the permeability-porosity relation (Eq. (A.3)). At the bottom of the melting column, the channel melt composition is the same as the matrix melt composition, viz.,

$$C_f^{ch}(0,t) = C_f^m(0,t) = \frac{C_s^0(t)}{k_m^0}. \tag{B.9}$$

The amount of stretching experienced by the frontside of the enriched signal is given by:

$$\frac{h_{stretched}^{channel}}{h_0} = \left(\frac{1-\psi}{\psi}\mathbb{R}\right)^{\frac{n-1}{n}} \frac{F_{\max}}{\phi_{ref}}. \tag{B.10}$$

For $\phi_{ref} = 0.02$, $F_{\max} = 15\%$, and other parameters listed above, the channel stretching factor is 30 which is significantly larger than the stretching factors for trace elements in the matrix.

Appendix C. Case of a linear melting rate: $\Gamma_m = 2G_m^0 z_0 z$

In this case, the degree of melting increases parabolically as a function of the vertical coordinate z:

$$F = \frac{G_m^0 z_0^2}{\rho_s V_s^0} z^2 = F_{\max} z^2, \tag{C.1}$$

where G_m^0 is a constant; z_0 is the height of the column where melting takes place; and $0 \le z \le 1$. Substituting Eq. (C.1) into Eq. (6), we can solve the matrix melt composition following the procedure and simplifications outlined in Section 2 and Appendix B. For modal melting, we have the following expressions for the matrix melt composition:

$$C_f^m(t,z) = \frac{C_s^0(t-t_f)}{k_m}\left[\frac{k_m + (1-k_m-\mathbb{R})F}{k_m}\right]^{\frac{k_m-1}{1-k_m-\mathbb{R}}}, \tag{C.2a}$$

$$\begin{aligned} t_f = {} & \sqrt{\frac{k_m}{F_{\max}(1-k_m-\mathbb{R})}}\, \operatorname{atan}\left(z\sqrt{\frac{F_{\max}(1-k_m-\mathbb{R})}{k_m}}\right) \\ & + \frac{\phi_0}{2F_{\max}(1-k_m-\mathbb{R})} \ln\left[\frac{k_m + F_{\max}(1-k_m-\mathbb{R})z^2}{k_m}\right], \end{aligned} \tag{C.2b}$$

where atan is the inverse tangent function.

Appendix D. Supplementary material

Supplementary material related to this article can be found online at https://doi.org/10.1016/j.epsl.2018.06.042.

References

Albarède, F., 1995. Introduction to Geochemical Modeling. Cambridge University Press.

Asimow, P.D., 1999. A model that reconciles major- and trace-element data from abyssal peridotites. Earth Planet. Sci. Lett. 169, 303–319.

Asimow, P.D., Stolper, E.M., 1999. Steady-state mantle–melt interactions in one dimension, I: equilibrium transport and melt focusing. J. Petrol. 40, 475–494.

Asimow, P.D., Hirschmann, M.M., Stolper, E.M., 1997. An analysis of variations in isentropic melt productivity. Philos. Trans. R. Soc. Lond. A 355, 255–281.

Barcilon, V., Richter, F.M., 1986. Nonlinear waves in compacting media. J. Fluid Mech. 164, 429–448.

Beck, A.R., Morgan, Z.T., Liang, Y., Hess, P.C., 2006. Dunite channels as viable pathways for mare basalt transport in the deep lunar mantle. Geophys. Res. Lett. 33, L01202. https://doi.org/10.1029/2005GL024008.

Bodinier, J.L., Vasseur, G., Vernieres, J., Dupuy, C., Fabries, J., 1990. Mechanisms of mantle metasomatism: geochemical evidence from the Lherz orogenic peridotite. J. Petrol. 31, 597–628.

Brunelli, D., Seyler, M., Cipriani, A., Ottolini, L., Bonatti, E., 2006. Discontinuous melt extraction and weak refertilization of mantle peridotites at the vema lithospheric section (Mid-Atlantic Ridge). J. Petrol. 47, 745–771.

DePaolo, D.J., 1996. High-frequency isotopic variations in the Mauna Kea tholeiitic basalt sequence: melt zone dispersivity and chromatography. J. Geophys. Res., Solid Earth 101, 11855–11864.

Hauri, E.H., 1997. Melt migration and mantle chromatography, 1: simplified theory and conditions for chemical and isotopic decoupling. Earth Planet. Sci. Lett. 153, 1–19.

Hellebrand, E., Snow, J.E., Hoppe, P., Hofmann, A.W., 2002. Garnet-field melting and late-stage refertilization in 'residual' abyssal peridotites from the Central Indian Ridge. J. Petrol. 43, 2305–2338.

Hesse, M.A., Schiemenz, A.R., Liang, Y., Parmentier, E.M., 2011. Compaction-dissolution waves in an upwelling mantle column. Geophys. J. Int. 187, 1057–1075.

Hewitt, I.J., Fowler, A.C., 2008. Partial melting in an upwelling mantle column. Proc. R. Soc., Math. Phys. Eng. Sci. 464, 2467–2491.

Iwamori, H., 1993a. Dynamic disequilibrium melting model with porous flow and diffusion-controlled chemical equilibration. Earth Planet. Sci. Lett. 114, 301–313.

Iwamori, H., 1993b. A model for disequilibrium mantle melting incorporating melt transport by porous and channel flows. Nature 366, 734–737.

Iwamori, H., 1994. ^{238}U–^{230}Th–^{226}Ra and ^{235}U–^{231}Pa disequilibria produced by mantle melting with porous and channel flows. Earth Planet. Sci. Lett. 125, 1–16.

Johnson, K.T.M., Dick, H.J.B., 1992. Open system melting and temporal and spatial variation of peridotite and basalt at the Atlantis II Fracture Zone. J. Geophys. Res., Solid Earth 97, 9219–9241.

Johnson, K.T.M., Dick, H.J.B., Shimizu, N., 1990. Melting in the oceanic upper mantle: an ion microprobe study of diopsides in abyssal peridotites. J. Geophys. Res., Solid Earth 95, 2661–2678.

Jordan, J.S., Hesse, M.A., Rudge, J.F., 2018. On mass transport in porosity waves. Earth Planet. Sci. Lett. 485, 65–78.

Jull, M., Kelemen, P.B., Sims, K., 2002. Consequences of diffuse and channelled porous melt migration on uranium series disequilibria. Geochim. Cosmochim. Acta 66, 4133–4148.

Kelemen, P.B., 1990. Reaction between ultramafic rock and fractionating basaltic magma, I: phase relations, the origin of calc-alkaline magma series, and the formation of discordant dunite. J. Petrol. 31, 51–98.

Kelemen, P.B., Hirth, G., Shimizu, N., Spiegelman, M., Dick, H.J.B., 1997. A review of melt migration processes in the adiabatically upwelling mantle beneath oceanic spreading ridges. Philos. Trans. R. Soc., Math. Phys. Eng. Sci. 355, 283–318.

Lambart, S., Laporte, D., Schiano, P., 2009. An experimental study of focused magma transport and basalt–peridotite interactions beneath mid-ocean ridges: implications for the generation of primitive MORB compositions. Contrib. Mineral. Petrol. 157, 429–451.

Langmuir, C.H., Bender, J.F., Bence, A.E., Hanson, G.N., Taylor, S.R., 1977. Petrogenesis of basalts from the FAMOUS area: Mid-Atlantic Ridge. Earth Planet. Sci. Lett. 36, 133–156.

Liang, Y., 2008. Simple models for dynamic melting in an upwelling heterogeneous mantle column: analytical solutions. Geochim. Cosmochim. Acta 72, 3804–3821.

Liang, Y., Liu, B., 2016. Simple models for disequilibrium fractional melting and batch melting with application to REE fractionation in abyssal peridotites. Geochim. Cosmochim. Acta 173, 181–197.

Liang, Y., Parmentier, E.M., 2010. A two-porosity double lithology model for partial melting, melt transport and melt–rock reaction in the mantle: mass conservation equations and trace element transport. J. Petrol. 51, 125–152.

Liang, Y., Peng, Q., 2010. Non-modal melting in an upwelling mantle column: steady-state models with applications to REE depletion in abyssal peridotites and the dynamics of melt migration in the mantle. Geochim. Cosmochim. Acta 74, 321–339.

Liang, Y., Schiemenz, A., Hesse, M.A., Parmentier, E.M., 2011. Waves, channels, and the preservation of chemical heterogeneities during melt migration in the mantle. Geophys. Res. Lett. 38.

Liu, B., Liang, Y., 2017a. An introduction of Markov chain Monte Carlo method to geochemical inverse problems: reading melting parameters from REE abundances in abyssal peridotites. Geochim. Cosmochim. Acta 203, 216–234.

Liu, B., Liang, Y., 2017b. The prevalence of kilometer-scale heterogeneity in the source region of MORB upper mantle. Sci. Adv. 3, e1701872.

Lundstrom, C., 2000. Models of U-series disequilibria generation in MORB: the effects of two scales of melt porosity. Phys. Earth Planet. Inter. 121, 189–204.

McKenzie, D., 1984. The generation and compaction of partially molten rock. J. Petrol. 25, 713–765.

Navon, O., Stolper, E., 1987. Geochemical consequences of melt percolation: the upper mantle as a chromatographic column. J. Geol. 95, 285–307.

Ozawa, K., 2001. Mass balance equations for open magmatic systems: trace element behavior and its application to open system melting in the upper mantle. J. Geophys. Res., Solid Earth 106, 13407–13434.

Qin, Z., 1992. Disequilibrium partial melting model and its implications for trace element fractionations during mantle melting. Earth Planet. Sci. Lett. 112, 75–90.

Ribe, N.M., 1985a. The deformation and compaction of partial molten zones. Geophys. J. Int. 83, 487–501.

Ribe, N.M., 1985b. The generation and composition of partial melts in the earth's mantle. Earth Planet. Sci. Lett. 73, 361–376.

Richter, F.M., Daly, S.F., 1989. Dynamical and chemical effects of melting a heterogeneous source. J. Geophys. Res., Solid Earth 94, 12499–12510.

Shaw, D.M., 2000. Continuous (dynamic) melting theory revisited. Can. Mineral. 38, 1041–1063.

Shaw, D.M., 2006. Trace Elements in Magmas: A Theoretical Treatment. Cambridge University Press.

Spiegelman, M., 1996. Geochemical consequences of melt transport in 2-D: the sensitivity of trace elements to mantle dynamics. Earth Planet. Sci. Lett. 139, 115–132.

Spiegelman, M., Elliott, T., 1993. Consequences of melt transport for uranium series disequilibrium in young lavas. Earth Planet. Sci. Lett. 118, 1–20.

Van Orman, J.A., Grove, T.L., Shimizu, N., 2002. Diffusive fractionation of trace elements during production and transport of melt in Earth's upper mantle. Earth Planet. Sci. Lett. 198, 93–112.

Walter, M., 2003. Melt extraction and compositional variability in mantle lithosphere. In: Treatise on Geochemistry, vol. 2, pp. 363–394.

Warren, J.M., 2016. Global variations in abyssal peridotite compositions. Lithos 248–251, 193–219.

Watson, S., Spiegelman, M., 1994. Geochemical effects of magmatic solitary wavers – I. Numerical results. Geophys. J. Int. 117, 284–295.

Workman, R.K., Hart, S.R., 2005. Major and trace element composition of the depleted MORB mantle (DMM). Earth Planet. Sci. Lett. 231, 53–72.

Yaxley, G.M., Green, D.H., 1998. Reactions between eclogite and peridotite: mantle refertilisation by subduction of oceanic crust. Schweiz. Mineral. Petrogr. Mitt. 78, 243–255.

Zou, H., 1998. Trace element fractionation during modal and nonmodal dynamic melting and open-system melting: a mathematical treatment. Geochim. Cosmochim. Acta 62, 1937–1945.

Zou, H., 2007. Quantitative Geochemistry. World Scientific.